A 2-D Hybrid Hall Thruster Simulation That Resolves the $\boldsymbol{E}\times\boldsymbol{B}$ Electron Drift Direction

Cheryl M. Lam, Eduardo Fernandez, and Mark A. Cappelli

***Abstract*— A 2-D axial–azimuthal model of an annular Hall thruster discharge is developed. We use a hybrid fluid–particle-in-cell (PIC) treatment to model a Xe-propellant Hall thruster. Using a PIC approach, the positive Xe+ ions are modeled as collisionless, nonmagnetized, discrete super-particles, whereas the electrons are treated as a magnetized 2-D fluid. The model includes a continuously replenished Xe neutral background, with an imposed radial magnetic field and an applied axial electric potential. Motivated by experimental evidence of anomalously high electron mobility across the magnetic field that has been attributed to quasi-coherent fluctuations in the plasma properties, we use the numerical model to resolve azimuthal electron dynamics and study the impact of fluctuations on electron transport. Representative low-voltage (100 V) operating condition simulations predict localized plasma properties similar to those observed in experiments. The simulations predict coherent azimuthally propagating disturbances which appear to contribute to enhanced electron transport beyond that due to classical scattering.**

***Index Terms*— Anomalous transport, Hall thrusters, hybrid simulations, simulations.**

I. Introduction

THE possibility of anomalously high electron mobility across the magnetic field has been experimentally documented since the early years of Hall thruster development [1], [2]. The mechanism leading to this anomalous mobility remains as one of the key challenges in Hall thruster research. Lack of understanding of what generates anomalous mobility in some regions of the flow, while being very near classical in other regions, has curtailed the usefulness of certain 2-D hybrid simulations [3]–[5].

Some theories attribute the anomalously high cross-field electron mobility to quasi-coherent fluctuations resulting from instabilities within the plasma [1], [4], [6]. There is also recent experimental evidence of coherent azimuthally propagating fluctuations which may contribute to the observed enhanced cross-field transport [2], [7], [8].

Manuscript received December 2, 2013; revised May 22, 2014 and July 25, 2014; accepted September 1, 2014. Date of publication October 14, 2014; date of current version January 6, 2015. The work of C. M. Lam was supported by Sandia National Laboratories, Livermore, CA, USA.

C. M. Lam and M. A. Cappelli are with the Stanford Plasma Physics Laboratory, Department of Mechanical Engineering, Stanford University, Stanford, CA 94305 USA (e-mail: cheryl16@stanford.edu; cap@stanford.edu).

E. Fernandez is with the Department of Mathematics and Physics, Eckerd College, St. Petersburg, FL 33711 USA (e-mail: fernane@eckerd.edu).

Color versions of one or more of the figures in this paper are available online at http://ieeexplore.ieee.org.

Digital Object Identifier 10.1109/TPS.2014.2356650

We have developed a global model that treats the azimuthal dynamics self-consistently [9]–[11]. We use the model to resolve the electron dynamics in the azimuthal direction, that is, as projected onto the axial–azimuthal (z–θ) plane, and focus on understanding the role played by fluctuations, particularly those that propagate with components perpendicular to both the applied electric ($\boldsymbol{E}$) and magnetic ($\boldsymbol{B}$) fields. In this paper, we describe the model in detail and discuss results for representative Hall thruster simulations. We use the numerical simulations to characterize oscillations, particularly in the $\boldsymbol{E}\times\boldsymbol{B}$ electron drift direction, and quantify their impact on the electron transport process, while making qualitative comparisons with experimentally observed phenomena.

II. Model Description

The 2-D axial–azimuthal (z–θ) model described here is similar to the previous hybrid fluid–particle-in-cell (PIC) Hall thruster models [4], [12], [13] developed in the radial–axial (r–z) plane. The heavy species, Xe and Xe+, are modeled using a PIC treatment, whereas the electrons are treated as a 2-D fluid continuum. The PIC and fluid treatments are coupled by assuming space charge neutrality, or quasineutrality, consistent with modeling large-scale phenomena, as the Debye length of the typical Hall thruster plasma is smaller than the length scales of interest [14].

A. Model Geometry and Computational Domain

The 2-D computational domain is constructed in the axial–azimuthal (z–θ) plane, starting with the anode region and extending beyond the exit plane into the discharge plume, and including the full azimuth (0–2π radians), as shown in Fig. 1; as far as we know, this is among the first z–θ-resolved simulations of an *entire thruster* that is carried out without an *ad hoc* scaling as is often done in full PIC simulations.

The geometry simulated is that of a laboratory Hall discharge, known as the Stanford Hall thruster (SHT), for which a considerable amount of experimental data has been gathered [2], [15]. While we focus here on simulations of the SHT, the model can be adapted to simulate other thruster geometries. The simulated SHT discharge has an annular thruster channel 8 cm in length and 1.2 cm in width, and an outer diameter of approximately 9 cm. The imposed constant magnetic field is based on experimental measurements of the predominantly radial magnetic field strength along the SHT

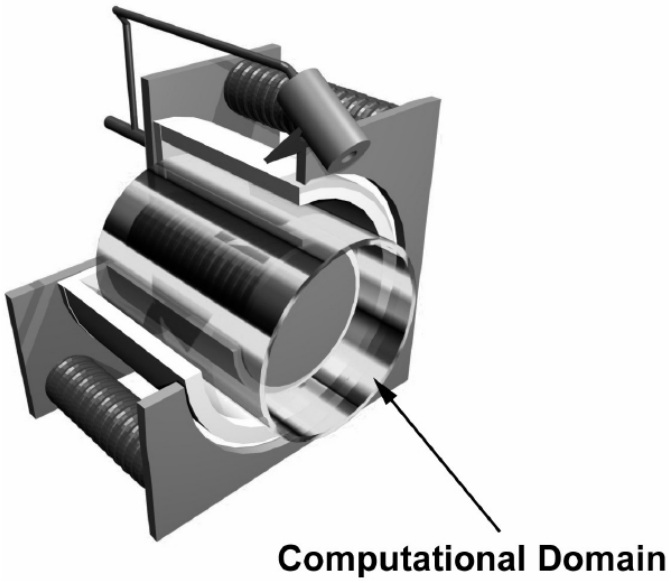

Fig. 1. Schematic of the modeled thruster and the computational domain.

z-axis at a midway radial location; it peaks at a value of approximately $B_r = 0.01$ T just upstream of the channel exit.

The axial electric field is imposed by a positive voltage (relative to 0 V) applied at the anode. We treat the magnetic field as purely radial, which leads to an $\boldsymbol{E} \times \boldsymbol{B}$ drift velocity in the purely azimuthal direction. The model's 2-D z–θ coordinate system is oriented such that the $\boldsymbol{E} \times \boldsymbol{B}$ drift velocity is in the positive θ-direction.

The model does not include any radial dynamics; as such, particle collisions with the inner and outer radial thruster walls, including wall scattering and ion recombination, are not explicitly modeled. Instead, wall collision effects, such as neutral axial flow resistance and electron fluid energy losses to the wall, are modeled in an *ad hoc* manner.

B. Neutral Gas

Neutral Xe atoms are modeled as collisonless, discrete super-particles. Neutral atoms are continuously injected into the domain from the anode ($z = 0$) plane according to the prescribed mass flow rate. To account for the effect of wall collisions which are not explicitly modeled here, the neutral injection velocity is sampled from a half-Maxwellian distribution, centered at a mean speed chosen to best match conditions seen along the channel centerline in similar r–z simulations [13] which do include wall collision effects.

C. Ions

Singly charged Xe+ ions are created by ionizing neutral Xe atoms according to the local electron–neutral impact ionization rate. The ionization rate depends nonlinearly on electron temperature; we assume a Maxwellian distribution for the electrons and use an analytical expression for the ionization rate [16] based on fits to experimental cross sections [17], [18].

The Xe+ ions are modeled as collisionless, discrete super-particles by using a PIC treatment. Because of the relatively large ion mass, and consequently large Larmor radius relative to the length scales of interest, the effect of the magnetic field on the ions is neglected. The ions are subject to the locally computed electric field per the PIC treatment.

D. Electron Fluid

The electrons are modeled as a 2-D inertialess fluid. The electron fluid is governed by current conservation, per the assumed electron–ion quasineutrality, and the first three moments of the Boltzmann equation (continuity, momentum, and energy equations).

The electron momentum is described using the drift-diffusion approximation. The model has two cross-field electron velocity components, one in the axial direction, and the other in the azimuthal direction

$$u_{\mathrm{ez}} = -\mu_\perp E_z - \frac{D_\perp}{n_e}\frac{\partial n_e}{\partial z} - \frac{D_\perp}{T_e}\frac{\partial T_e}{\partial z} - \frac{1}{1+\left(\frac{\nu_{\mathrm{en}}}{\omega_{\mathrm{ce}}}\right)^2}\frac{E_\theta}{B_r} - \frac{1}{1+\left(\frac{\nu_{\mathrm{en}}}{\omega_{\mathrm{ce}}}\right)^2}\frac{kT_e}{en_eB_r r}\frac{\partial n_e}{\partial \theta} \tag{1.1}$$

$$u_{e\theta} = -\mu_\perp E_\theta - \frac{D_\perp}{n_e r}\frac{\partial n_e}{\partial \theta} + \frac{1}{1+\left(\frac{\nu_{\mathrm{en}}}{\omega_{\mathrm{ce}}}\right)^2}\frac{E_z}{B_r} + \frac{1}{1+\left(\frac{\nu_{\mathrm{en}}}{\omega_{\mathrm{ce}}}\right)^2}\frac{kT_e}{en_eB_r}\frac{\partial n_e}{\partial z} + \frac{1}{1+\left(\frac{\nu_{\mathrm{en}}}{\omega_{\mathrm{ce}}}\right)^2}\frac{k}{eB_r}\frac{\partial T_e}{\partial z} \tag{1.2}$$

where $k = 1.38 \times 10^{-23}$ m$^2 \cdot$ kg $\cdot$ s$^{-2} \cdot$ K^{-1} is the Boltzmann constant, $e = 1.6 \times 10^{-19}$ C is the elementary electron charge, n_e is the electron number density, T_e is the electron temperature, B_r is the radial magnetic field strength, and E_z and E_θ are the axial and azimuthal components, respectively, of the electric field; ν_{en} is the electron–neutral collision frequency as described in [16], ω_{ce} is the electron cyclotron frequency, and we use the classical electron mobility and diffusion coefficient

$$\mu_\perp = \frac{e}{m_e\nu_{\mathrm{en}}\left[1+\left(\frac{\omega_{\mathrm{ce}}}{\nu_{\mathrm{en}}}\right)^2\right]} \tag{2.1}$$

$$D_\perp = \frac{kT_e}{e}\mu_\perp \tag{2.2}$$

where $m_e = 9.1 \times 10^{-31}$ kg is the elementary electron mass.

To see how fluctuation-induced transport can occur, we note that the axial electron velocity has a fluctuating $\boldsymbol{E} \times \boldsymbol{B}$ term arising from azimuthal electric field perturbations. If the fluctuating plasma density is properly correlated with this fluctuating velocity, transport will result.

Electron energy is described by a time-dependent equation

$$\frac{3}{2}n_ek\left(\frac{\partial T_e}{\partial t} + \vec{u}_e \cdot \nabla T_e\right) + n_ekT_e\nabla\cdot\vec{u}_e - \nabla\cdot\vec{q}_e = S_{\mathrm{joule}} - S_{\mathrm{ioniz}} - S_{\mathrm{wall}} \tag{3}$$

where $\boldsymbol{q}_e$ is the electron heat flux. We include convective and diffusive fluxes, as well as joule heating, ionization losses, and

an effective wall loss

$$S_{\text{joule}} = m_e n_e \nu_{\text{en}} \left\| \vec{u_e} \right\|^2 \tag{4.1}$$

$$S_{\text{ioniz}} = \dot{n}_e e_i k + \dot{n}_e \frac{3}{2} k T_e \tag{4.2}$$

$$S_{\text{wall}} = e\dot{n}_{\text{wall}} \left[\frac{2kT_e}{e(1-\delta)} + \phi_w \right] \tag{4.3}$$

where $\dot{n}_e$ is the local ionization rate and e_i is the Xe first ionization energy. Equation (4.3) is derived from [19] and accounts for the electron fluxes into and out of the inner and outer radial channel walls; the ion loss (per unit volume) to the walls $\dot{n}_{\text{wall}}$ and the electric potential drop at the wall ϕ_w are defined as

$$\dot{n}_{\text{wall}} = 2\frac{n_e}{W} S(z) \upsilon_{\text{Bohm}} = 2\frac{n_e}{W} S(z) \exp(-0.5) \sqrt{\frac{kT_e}{m_i}} \tag{5.1}$$

$$\phi_w = \frac{kT_e}{e} \ln \left[(1-\delta) \frac{\exp(0.5)}{4} \sqrt{\frac{8m_i}{\pi m_e}} \right] \tag{5.2}$$

where m_i is the Xe^+ ion mass, $W = 0.012$ m is the thruster channel width, and $S(z)$ is a shape factor used to account for imperfect contact between the plasma and the walls as described in [19]. We use a value of $\delta = 0.3$ for the secondary emission coefficient and a constant shape factor $S(z) = S_0 = 0.009$. The electron energy equation is 1-D in z; the electron temperature is thus taken to be axisymmetric.

E. Numerical Solution Method

The neutral and ion particle positions and velocities are time-advanced using a leap frog method, with the ions subject to the interpolated electric field. We couple the ion and electron treatments via quasineutrality; we calculate the plasma number density per the ion PIC treatment and apply this PIC value to the electron fluid equations, using the same numerical grid for the PIC treatment and the electron fluid discretization. To mitigate the destabilizing effect of strong spatial variations in the PIC plasma number density and other derived plasma properties on the electron fluid equations, we apply a smoothing cubic spline interpolation to the PIC plasma properties prior to using these quantities and their derivatives in the electron fluid equations.

To obtain the 1-D form of the electron temperature equation, we consider the azimuthal average (i.e., average all relevant quantities over θ) for each z location; the time-dependent 1-D electron temperature equation is solved via a fourth-order Runge–Kutta method. The electric field is not solved from Poisson's equation (since quasineutrality is assumed); instead, the electric potential ϕ is obtained by solving a convection–diffusion equation that results from combining the current continuity and momentum equations and setting $n_e = n_i$. This equation takes the form

$$A_1 \frac{\partial^2 \phi}{\partial \theta^2} + A_2 \frac{\partial \phi}{\partial \theta} + A_3 \frac{\partial^2 \phi}{\partial z^2} + A_4 \frac{\partial \phi}{\partial z} + A_5 = 0 \tag{6}$$

where

$$\vec{E} = -\nabla \phi \tag{7}$$

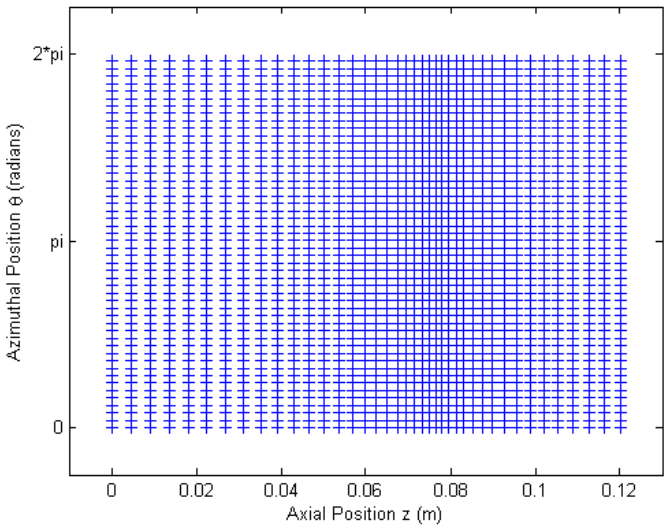

Fig. 2. Numerical grid resolution.

and the coefficients $\{A_1, A_2, \ldots, A_5\}$ are as defined in the Appendix.

The difficulty with (6) is the strong convection imposed by the electron $\boldsymbol{E} \times \boldsymbol{B}$ flow. We use a high-order upwind discretization method [20] to circumvent numerical instability. Such discretization results in a block-tridiagonal matrix for the electric potential that is solved via a direct-solve method.

The same time step is used to advance both the particle motion and the electron fluid equations. At each time step, neutrals are injected at the anode based on the mass flow rate. Neutrals are also ionized at each time step according to the local ionization rate. This sequence is repeated for the next time step after a steady-state for the mean quantities is obtained. The steady-state is nonstationary; sustained electric current discharge oscillations are a distinctive feature of the simulation.

The boundary conditions are periodic in the azimuthal direction. For the axial direction, we impose axisymmetric (constant in θ) Dirichlet boundary conditions at the axial domain boundaries. For the electric potential, we impose a voltage boundary condition based on the thruster operating condition; for the electron temperature, we enforce a zero-slope ($dT_e/dz = 0$) condition at the domain boundaries.

III. Results and Discussion

We present results for a representative simulation of low-voltage SHT operation. The simulated features and phenomena described here have also been observed in simulations of other (higher voltage) operating conditions for the same SHT geometry.

In an effort to balance spatial resolution and computational cost, we used a computational grid of 40 (axial) by 50 (azimuthal) points as shown in Fig. 2. The computational grid is nonuniform in the axial direction, with additional grid points clustered near the magnetic field peak, where gradients are expected to be large. The grid is uniform in the periodic azimuthal direction. The axial domain extends from the anode to 4 cm past the channel exit.

To approximately match experimental operating conditions, a neutral Xe injection mass flow rate of 2 mg/s was imposed. The simulation was performed for an operating voltage of 100 V, imposed at the anode. While the Dirichlet boundary condition at the anode is reasonable (the anode is at a fixed voltage), the downstream boundary condition is less clear; for this simulation, the electric potential was set to 30 V at the downstream domain boundary ($z = 0.12$ m) based on experimental measurements of the electric potential at that location (4 cm past the channel exit). The electric potential difference between the anode ($z = 0$) and downstream ($z = 0.12$ m) domain-end boundary conditions is thus 70 V; in both cases, the electric potential boundary condition is imposed axisymmetrically, that is, uniformly in θ.

The simulation was initialized by assigning a uniform number of super-particles to each cell, with the particles randomly distributed in position within each cell. The prescribed initial ion particle population was set to reflect a uniform ion number density of $n_i = 1.7 \times 10^{17}$ m^{-3} throughout the computational domain; the neutral population was initialized according to a neutral density profile which varied linearly from a peak value of approximately $n_n = 3.2 \times 10^{19}$ m^{-3} at the anode ($z = 0$) to $n_n = 1.6 \times 10^{19}$ m^{-3} at the downstream computational boundary ($z = 0.12$ m). The particle velocities were initialized by inverting a Maxwellian velocity distribution.

Note that the initial particle profiles are uniform in θ, that is, axisymmetric, and that we start the simulation from perfectly smooth neutral and ion density profiles. The objective was to allow the simulated fluctuations to arise naturally and evolve self-consistently; hence, we start from a fluctuation free initial condition.

A 200 μs simulation was performed using a time step of $dt = 1$ ns. The initial number of super-particles was 400 000 per particle species (Xe and Xe+). The simulation took approximately 6 days to complete on a single Intel Xeon x5355 2.66 GHz processor core.

A. General Results

We compare the simulation results with experimental measurements of plasma properties at the given operating conditions [15], [21], [22]. Fig. 3 shows the axial variation of various simulated plasma properties—electron number density (or plasma density), electric potential, electron temperature, and axial ion velocity—time-averaged over the simulated time duration 50–100 μs. In general, the simulated axial profiles show good qualitative agreement with experimental measurements.

Fig. 4(a) shows the simulated discharge current at an axial location just upstream of the channel exit; the simulation predicts a time-varying discharge current of approximately 1–2 A at this location. In experiments at this operating voltage, the measured discharge current was approximately 2 A.

Note that the discharge current varies, in some cases, significantly, with axial position as shown in Fig. 4(b). In this simulation, we see significant axial variation in the total discharge current, that is, significant current nonconservation, for $z \leq 0.04$ m as shown in Fig. 4(b). In the region $z \leq 0.04$ m, the total current varies by as much as 200% over a range of 3 A (approximately -0.5 A minimum, which would indicate an opposite flowing current, to 2.5 A maximum); in the region

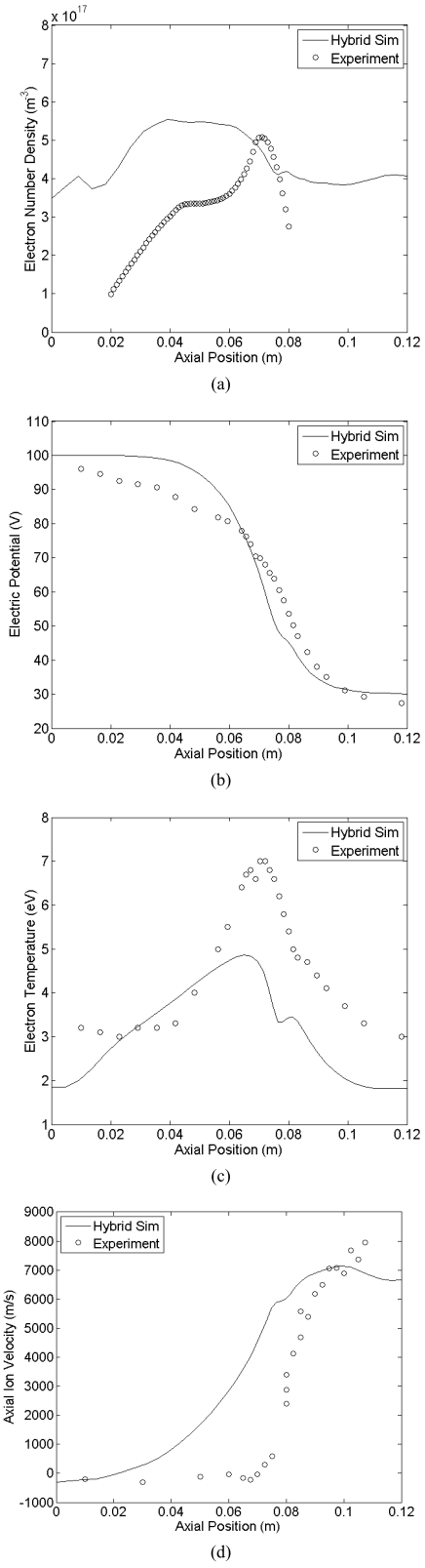

Fig. 3. Comparison of time-averaged axial profiles for various plasma properties. (a) Electron, or plasma, number density. (b) Electric potential. (c) Electron temperature. (d) Axial ion velocity.

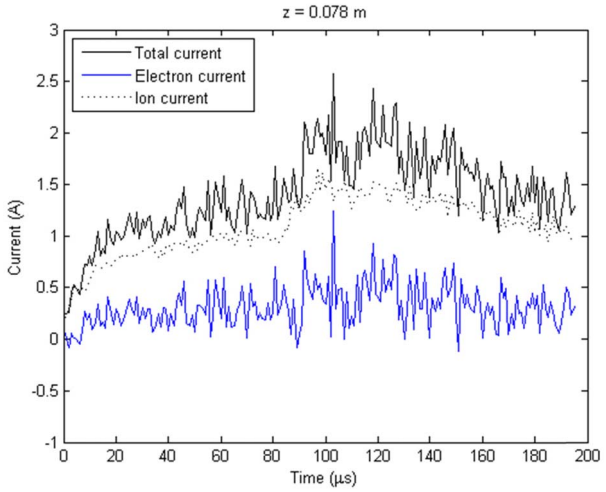

(a)

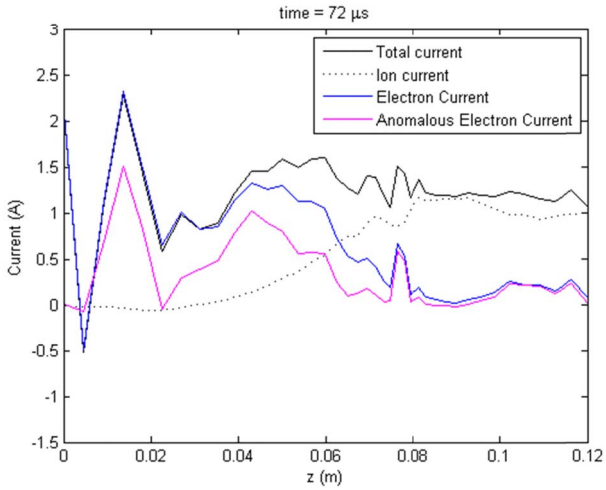

(b)

Fig. 4. Variation of the discharge current with time and axial location. (a) Discharge current time history at $z = 0.078$ m (just upstream of the thruster channel exit). (b) Snapshot of the axial variation of the discharge current (including the anomalous electron current contribution) for a representative point in simulated time.

$z > 0.04$ m, the total current is better conserved and varies minimally, by approximately 20%.

We believe the strong variation in the axial current for $z \leq 0.04$ m to be an artifact of the numerical scheme, grid resolution, and strong gradients in the plasma properties in this region. The imposition of the axisymmetric electric potential boundary condition at the anode ($z = 0$) leads to an effective boundary layer and strong gradients near the anode; without significantly finer (computationally expensive) grid resolution, such strong gradients can be difficult to resolve via a finite difference scheme [23], as employed here, and may contribute to the apparent lack of global current conservation in this region. Properly resolving the anode region, and the discharge current in this region, has historically been problematic for other similar hybrid simulations [13]; furthermore, in this region of weak magnetic field strength, there is little experimental data for comparison and validation. In general, the near anode region is less well described and more difficult to accurately simulate than other features of the thruster; thus, the variation in the predicted axial current is not surprising. The current is well conserved throughout the rest of the thruster channel and computational domain ($z > 0.04$ m) with the present numerical scheme and grid resolution.

B. Azimuthal Wave Propagation

Closer analysis of the simulation results reveals dispersive wave propagation. The extended time duration of the hybrid simulation allows for investigation of low- and mid-frequency fluctuations. We observe tilted waves which propagate simultaneously in the axial and azimuthal directions. The spatial structure, frequency, phase velocity, and propagation direction of these tilted waves appear to vary with axial position. Fig. 5(b) illustrates the spatial variation in wave structure. Fig. 5 shows a time snapshot and Figs. 6 through 8 show streak plots of the axial electron velocity to illustrate the spatial wave structure and variation of wave properties with axial position. Although not shown here, we observe similar wave structure, with axial position, in the plasma density and electric potential.

As shown in Fig. 5(b), we observe distinct wave behavior in three distinct axial regions. For most of the thruster channel, starting just downstream of the anode to just upstream of the channel exit plane (approximately, 0.01 m $\leq z \leq$ 0.07 m), we observe tilted waves, propagating in the negative z- and positive θ-directions. A representative streak plot (Fig. 6) in this axial region reveals the time variation of the wave structure. These waves have an azimuthal wavelength on the order of 5 cm and a linear frequency of approximately 40 kHz; the phase velocity is approximately 4000 m/s. These waves are low frequency and slow moving, and travel in the $+\boldsymbol{E} \times \boldsymbol{B}$ direction.

In a narrow axial region (approximately, 0.07 m $\leq z \leq$ 0.08 m), starting just upstream of the thruster channel exit plane through the exit plane itself, we observe higher frequency, tilted waves traveling in the positive z- and negative θ-directions. Over long time scales, as shown in Fig. 7(a), the coherent wave structure cannot be discerned; instead, the behavior appears turbulent with indiscernible high frequency structure. Examination at shorter time scales, as in Fig. 7(b), however, reveals fast-moving waves. These waves have an azimuthal wavelength on the order of 4 cm and a linear frequency on the order of 600–700 kHz; the phase velocity is approximately 40 000 m/s. These waves are shorter wavelength, higher frequency and faster moving (than the waves in the upstream region 0.01 m $\leq z \leq$ 0.07 m); they travel in the $-\boldsymbol{E} \times \boldsymbol{B}$ direction. We note that this axial region corresponds to the region of peak magnetic field strength; as shown in Fig. 5(c), there is also a strong fluctuation and two opposite extremums (local maximum and local minimum) in the axial shear (of the azimuthal electron velocity) in this region. As shown in Fig. 5(a), this is also the region in which the gradient of n_e/B_r becomes positive; that is, the quantity n_e/B_r starts to increase near $z = 0.075$ m.

Just outside the exit plane, the wave structure is unclear. From approximately 10 cm past the exit plane through the end of the computational domain ($z > 0.01$ m), however, we observe azimuthally standing waves that are propagating

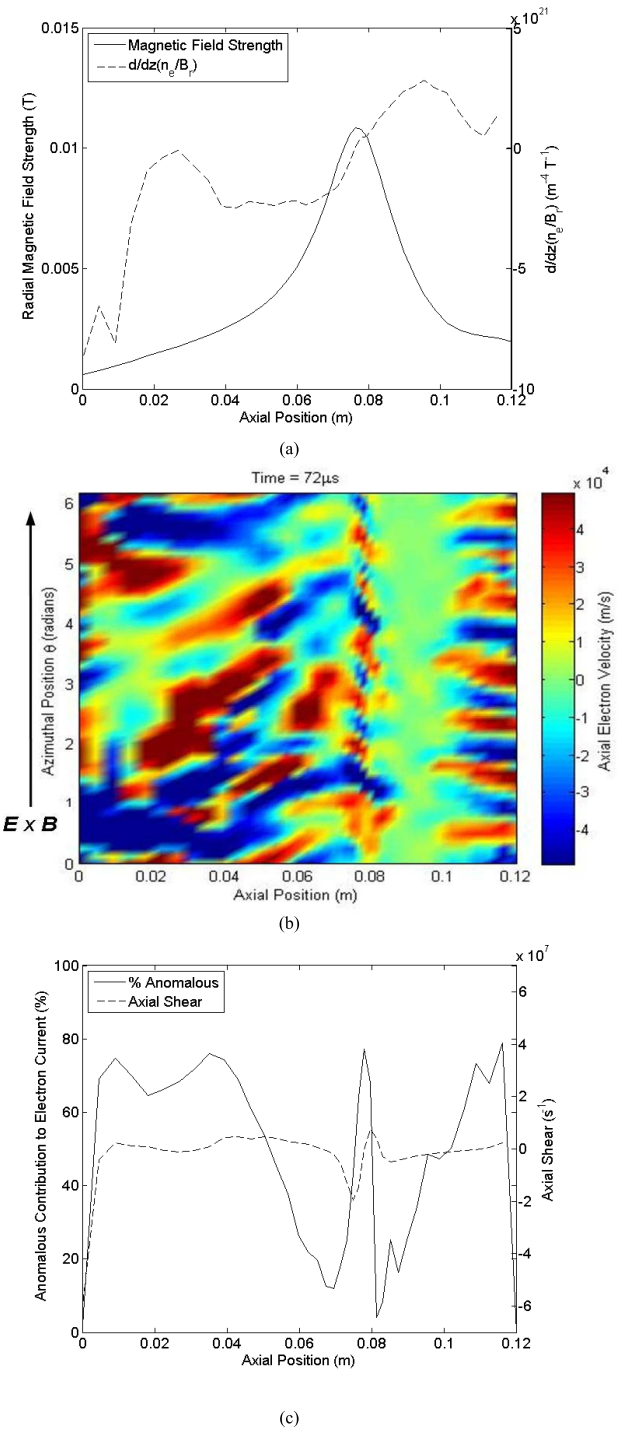

Fig. 5. (a) Axial variation of the magnetic field strength B_r and the axial gradient of n_e/B_r, shown for reference. (b) Typical time snapshot of the axial electron velocity illustrates the spatial structure of the wave propagation. (c) Axial variation of the anomalous (azimuthal-fluctuation driven) contribution to the electron transport, time-averaged over the duration 50–100 μs, as related to the axial shear $\partial u_{e\theta}/\partial z$.

in the purely axial direction. These waves appear to have the same spatial structure and azimuthal wavelength as the waves just inside (and leaving) the thruster exit plane; they propagate in the positive z direction. A representative streak plot, as shown in Fig. 8, confirms the time persistence and purely axial nature of these waves.

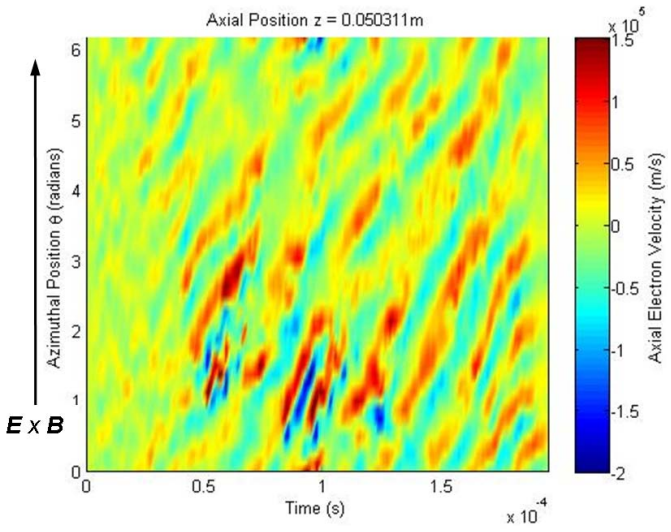

Fig. 6. Axial electron velocity streak plot at axial location $z = 0.05031$ m.

As detailed here, the wave structure varies distinctly with axial location; these changes in wave structure appear to be coincident with the axial variation of the magnetic field strength, axial shear, and gradient of n_e/B_r. The longer wavelength, lower frequency tilted waves, propagating in the negative z and $+\boldsymbol{E} \times \boldsymbol{B}$ direction in the upstream axial region (0.01 m $\leq z \leq$ 0.07 m), coincide with a region of high neutral particle density, increasing magnetic field strength, and low axial variation in the shear. Their relatively low propagation velocity and long wavelength, with hints of $m = 1, 2$ azimuthal mode structure for $z < 0.04$ m [see Fig. 5(b)], suggests that these may be so-called spoke instabilities, perhaps related to the Simon instability associated with weakly ionized plasmas in magnetic fields with density gradients [24].

At approximately $z = 0.07$ m, the waves reverse both axial and azimuthal propagation direction; the wavelength decreases, as the frequency and phase velocity increase by approximately one order of magnitude. As previously noted, these waves are coincident with peak magnetic field strength, strong axial variation in the axial shear, and a change in sign of the n_e/B_r gradient. Their frequencies, approaching 1 MHz, suggest that these waves are related to the so-called ion transit-time instabilities [25], named accordingly because their period is approximately the transit time of the ions across the region of acceleration.

The azimuthal spatial wave structure is preserved as the waves are advected out of the thruster channel. Purely axial waves, propagating in the positive axial direction, can be observed downstream of the exit plane (for $z \geq 0.1$ m); these waves appear to have the same azimuthal wavelength as those leaving the channel exit plane. The standing nature of these waves suggests that they are the result of a two-stream instability arising from the interactions between the drifting electrons from the cathode and the accelerated ions as the ions leave the thruster. These waves, originating near the exit of the thruster, have been thought to be related to the anomalous erosion seen in Hall thrusters [26].

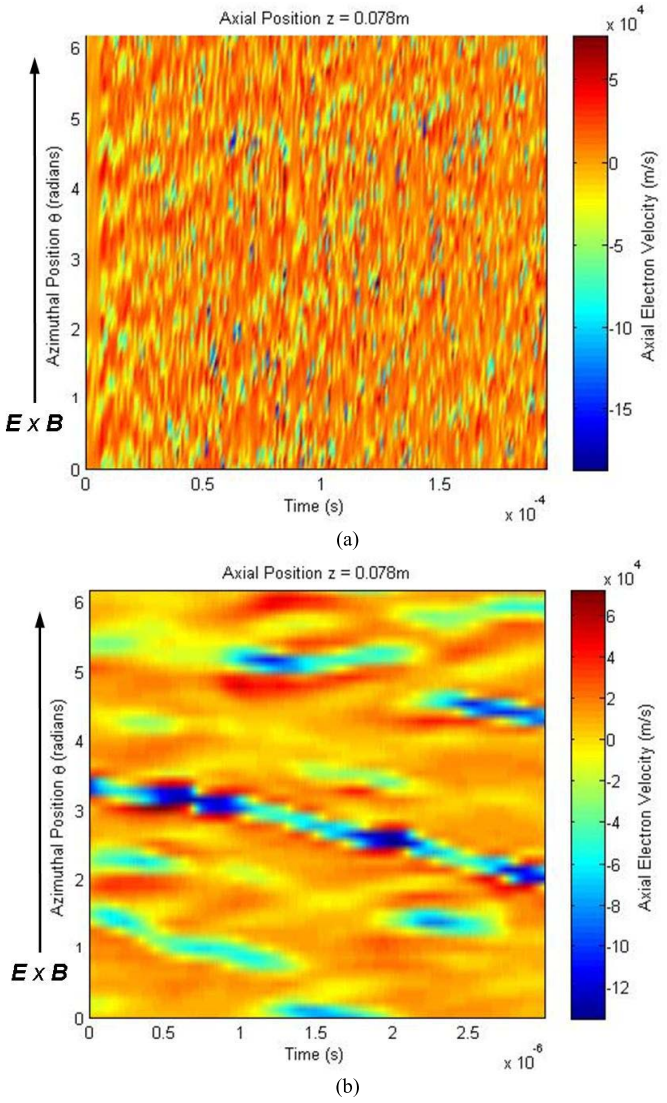

Fig. 7. Axial electron velocity streak plot at axial location $z = 0.078$ m, shown at different time scales. (a) Full 200 μs simulation time duration at low time-resolution. (b) Time duration of 3 μs at higher time-resolution (ns sampling rate).

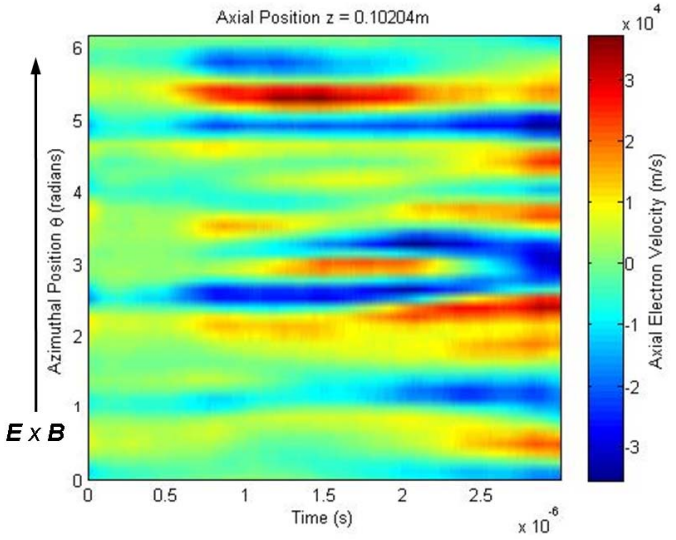

Fig. 8. Axial electron velocity streak plot at axial location $z = 0.102$ m, shown at high time-resolution (ns sampling rate) over a time duration of 3 μs.

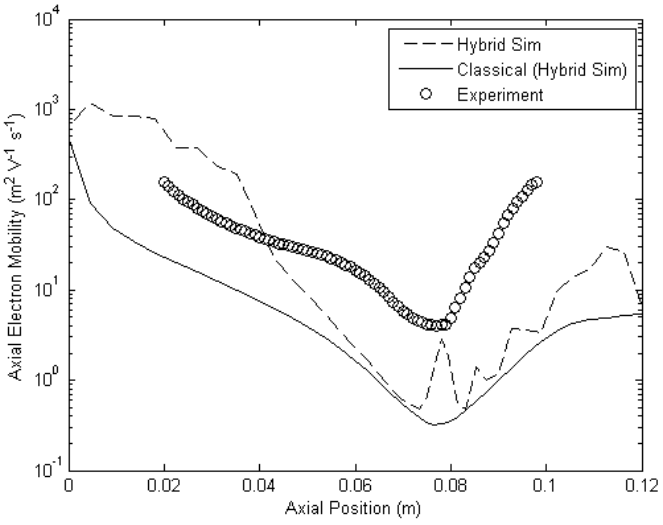

Fig. 9. Simulated electron axial mobility, as compared to experimentally measured and classically predicted values.

Although the attribution of these various waves to specific physical mechanisms or observed experimental phenomena is difficult, it is noteworthy that the simulation predicts a very rich dynamical behavior throughout the discharge channel for this extended length Hall discharge.

C. Electron Transport

We are interested in the impact of azimuthal fluctuations on axial electron transport. Experimental measurements indicate an axial electron mobility significantly higher than that predicted by classical theory. It has been proposed that correlated fluctuations in the plasma density and electron velocity can enhance the axial electron mobility.

Fig. 5(c) shows the so-called anomalous contribution to the electron current which arises from the E_θ and $\partial n_e/\partial\theta$ terms (last two terms) in (1.1). Note that where the axial variation in the azimuthal electron velocity (axial shear) is strongest, that is, largest in magnitude, the anomalous contribution to the electron current is at its minimum. Just upstream of the exit plane, where the magnitude of the axial shear is at its minimum, there is a peak in the anomalous contribution to the electron current; this region also coincides with that of the higher frequency (600–700 kHz), shorter wavelength ($k_\theta \approx 4$ cm) fluctuations. We speculate that the correlation between the reduction in transport and the magnitude of the axial shear is not a coincidence, and that the axial shear serves to disrupt the strong correlated fluctuations that give rise to the transport in this region of the thruster.

In Fig. 9, we compare the simulated axial electron mobility to that measured experimentally. We define the simulated axial electron mobility

$$\mu(z) = \frac{J_{\mathrm{ez}}}{\mathrm{e}n_e E_z} \tag{8}$$

where J_{ez} is the electron current density, summed or averaged across all θ for that z location, $e = 1.6 \times 10^{-19}$ C, and

n_e and E_z are the $\theta-$averaged (i.e., averaged across all θ for that z) electron number density and axial electric field, respectively. The classical mobility as defined in (2.1), calculated using the simulated neutral number density and electron temperature, is also shown for reference. In all cases, the plasma properties have been time-averaged over the simulated time duration 50–100 μs.

The simulated fluctuations in plasma density and electron velocity appear to have significant impact on the overall electron mobility. The electron mobility is significantly enhanced, compared to classical, at all axial locations; overall, the predicted mobility is of the same order of magnitude and shows good qualitative agreement with the experimentally observed values.

IV. Conclusion

The model developed and described here is intended as a tool to aid our fundamental understanding of how azimuthal fluctuations may impact electron transport. We believe the simulation presented here is among the first to resolve a full-scale (9 cm diameter) thruster, with the azimuthal scale resolved in its entirety. The time step and computational grid resolution chosen here enable simulation run times on the order of hundreds of μs, which allow us to study low- to mid-frequency, longer wavelength, and slowly propagating (low phase velocity) fluctuations.

The simulation predicts coherent fluctuations in the azimuthal, that is, the $\pm \boldsymbol{E} \times \boldsymbol{B}$ electron drift direction, that are generally complex. The simulation predicts an axial electron mobility that is significantly higher than that based on classical scattering; this predicted mobility is qualitatively comparable to that seen in experiments.

The simulation draws attention to the potential importance played by lower frequency (<1 MHz) fluctuations on transport. More importantly, the simulations confirm the correlation between this transport and the strong axial shear in the electron velocity near the region of strong magnetic field. The simulation provides first insight into the possible mechanism that this shear plays on reducing the transport to very low levels in this region of the thruster.

Appendix
Coefficients for Electric Potential Equation

The coefficients for the electric potential equation (6) are defined

$$A_1 = -\frac{n_e \mu_\perp}{r^2} \tag{A1}$$

$$A_2 = -\frac{1}{r}\left[\begin{array}{l} \frac{n_e}{r}\frac{\partial \mu_\perp}{\partial \theta} + \frac{\mu_\perp}{r}\frac{\partial n_e}{\partial \theta} + \frac{1}{1+\left(\frac{\nu_{\text{en}}}{\omega_{\text{ce}}}\right)^2}\frac{\partial}{\partial z}\left(\frac{n_e}{B_r}\right) \\ + \frac{n_e}{B_r}\frac{\partial}{\partial z}\left(\frac{1}{1+\left(\frac{\nu_{\text{en}}}{\omega_{\text{ce}}}\right)^2}\right) \end{array}\right] \tag{A2}$$

$$A_3 = -n_e \mu_\perp \tag{A3}$$

$$A_4 = \frac{1}{1+\left(\frac{\nu_{\text{en}}}{\omega_{\text{ce}}}\right)^2}\frac{1}{rB_r}\frac{\partial n_e}{\partial \theta} - n_e\frac{\partial \mu_\perp}{\partial z} - \mu_\perp \frac{\partial n_e}{\partial z} + \frac{n_e}{rB_r}\frac{\partial}{\partial \theta}\left(\frac{1}{1+\left(\frac{\nu_{\text{en}}}{\omega_{\text{ce}}}\right)^2}\right) \tag{A4}$$

$$A_5 = f(n_e, T_e, \mu_\perp, \nu_{\text{en}}, \omega_{\text{ce}}) + \frac{n_e}{r}\frac{\partial u_{i\theta}}{\partial \theta} + \frac{u_{i\theta}}{r}\frac{\partial n_e}{\partial \theta} + n_e\frac{\partial u_{iz}}{\partial z} + u_{iz}\frac{\partial n_e}{\partial z} \tag{A5}$$

where

$$\begin{aligned} f(n_e, T_e, \mu_\perp, \nu_{\text{en}}, \omega_{\text{ce}}) &= \frac{kT_e\mu_\perp}{er^2 n_e}\left(\frac{\partial n_e}{\partial \theta}\right)^2 + \frac{kT_e\mu_\perp}{en_e}\left(\frac{\partial n_e}{\partial z}\right)^2 \\ &+ \frac{n_e kT_e}{er^2}\left[\frac{1}{n_e}\frac{\partial \mu_\perp}{\partial \theta}\frac{\partial n_e}{\partial \theta} + \frac{\mu_\perp}{n_e^2}\left(n_e\frac{\partial^2 n_e}{\partial \theta^2} - \left(\frac{\partial n_e}{\partial \theta}\right)^2\right)\right] \\ &+ \frac{n_e kT_e}{e}\left[\frac{1}{n_e}\frac{\partial \mu_\perp}{\partial z}\frac{\partial n_e}{\partial z} + \frac{\mu_\perp}{n_e^2}\left(n_e\frac{\partial^2 n_e}{\partial z^2} - \left(\frac{\partial n_e}{\partial z}\right)^2\right)\right] \\ &- \frac{kT_e}{erB_r}\frac{\partial}{\partial \theta}\left(\frac{1}{1+\left(\frac{\nu_{\text{en}}}{\omega_{\text{ce}}}\right)^2}\right)\frac{\partial n_e}{\partial z} + \frac{kT_e}{erB_r}\frac{\partial}{\partial z}\left(\frac{1}{1+\left(\frac{\nu_{\text{en}}}{\omega_{\text{ce}}}\right)^2}\right)\frac{\partial n_e}{\partial \theta} \\ &- \frac{n_e k}{erB_r}\frac{\partial}{\partial \theta}\left(\frac{1}{1+\left(\frac{\nu_{\text{en}}}{\omega_{\text{ce}}}\right)^2}\right)\frac{\partial T_e}{\partial z} + 2\frac{k\mu_\perp}{e}\frac{\partial T_e}{\partial z}\frac{\partial n_e}{\partial z} \\ &- \frac{1}{1+\left(\frac{\nu_{\text{en}}}{\omega_{\text{ce}}}\right)^2}\frac{kT_e}{erB_r^2}\frac{\partial B_r}{\partial z}\frac{\partial n_e}{\partial \theta} \\ &+ \frac{n_e k}{e}\frac{\partial \mu_\perp}{\partial z}\frac{\partial T_e}{\partial z} + \frac{n_e k\mu_\perp}{e}\frac{\partial^2 T_e}{\partial z^2}. \end{aligned} \tag{A6}$$

References

[1] G. S. Janes and R. S. Lowder, "Anomalous electron diffusion and ion acceleration in a low-density plasma," *Phys. Fluids*, vol. 9, no. 6, pp. 1115–1123, 1966.

[2] N. B. Meezan, W. A. Hargus, Jr., and M. A. Cappelli, "Anomalous electron mobility in a coaxial Hall discharge plasma," *Phys. Rev. E*, vol. 63, no. 2, p. 026410, Jan. 2001.

[3] E. Fernandez, M. A. Cappelli, and K. Mahesh, "2D simulations of Hall thrusters," in *Center for Turbulence Research Annual Research Briefs*. Stanford, CA, USA: Stanford Univ., 1998, pp. 81–90.

[4] J. M. Fife, "Hybrid-PIC modeling and electrostatic probe survey of Hall thrusters," Ph.D. dissertation, Dept. Aeronautics Astronautics, Massachusetts Inst. Technol., Cambridge, MA, USA, 1999.

[5] G. J. M. Hagelaar, J. Bareilles, L. Garrigues, and J.-P. Boeuf, "Two-dimensional model of a stationary plasma thruster," *J. Appl. Phys.*, vol. 91, no. 9, pp. 5592–5598, 2002.

[6] S. Yoshikawa and D. J. Rose, "Anomalous diffusion of a plasma across a magnetic field," *Phys. Fluids*, vol. 5, no. 3, pp. 334–340, 1962.

[7] A. K. Knoll, "Plasma oscillations and associated electron transport within Hall thrusters," Ph.D. dissertation, Dept. Mech. Eng., Stanford Univ., Stanford, CA, USA, 2010.

[8] C. L. Ellison, Y. Raitses, and N. J. Fisch, "Cross-field electron transport induced by a rotating spoke in a cylindrical Hall thruster," *Phys. Plasmas*, vol. 19, no. 1, pp. 013503-1–013503-7, Jan. 2012.

[9] C. M. Lam, A. K. Knoll, M. A. Cappelli, and E. Fernandez, "Two-dimensional (z-θ) simulations of Hall thruster anomalous transport," presented at 31st Int. Electr. Propuls. Conf. (IEPC), Ann Arbor, MI, USA, Sep. 2009, pp. 1–10.

[10] E. Fernandez and M. A. Cappelli, "Azimuthal dynamics and transport in two dimensional Hall thruster hybrid model," presented at 53rd Annu. Meeting APS Division Plasma Phys., Nov. 2011.

[11] C. M. Lam, M. A. Cappelli, and E. Fernandez, "Two-dimensional simulations of coherent fluctuation-driven transport in a Hall thruster," presented at 33rd Int. Electr. Propuls. Conf. IEPC, Washington, DC, USA, Oct. 2013.

[12] M. K. Scharfe, N. Gascon, M. A. Cappelli, and E. Fernandez, "Comparison of hybrid Hall thruster model to experimental measurements,' *Phys. Plasmas*, vol. 13, no. 8, pp. 083505-1–083505-12, Aug. 2006.

[13] M. K. Scharfe, "Electron cross field transport modeling in radial-axial hybrid Hall thruster simulations," Ph.D. dissertation, Dept. Mech. Eng., Stanford Univ., Stanford, CA, USA, 2009.

[14] E. Chouieri, "Plasma oscillations in Hall thrusters," *Phys. Plasmas*, vol. 8, no. 4, pp. 1411–1426, 2001.

[15] W. A. Hargus, "Investigation of the plasma acceleration mechanism within a coaxial Hall thruster," Ph.D. dissertation, Dept. Mech. Eng., Stanford Univ., Stanford, CA, USA, 2001.

[16] E. Ahedo, P. Martinez-Cerezo, and M. Martinez-Sanchez, "One-dimensional model of the plasma flow in a Hall thruster," *Phys. Plasmas*, vol. 8, no. 6, pp. 3058–3068, 2001.

[17] D. Rapp and P. Englander-Golden, "Total cross sections for ionization and attachment in gases by electron impact. I. Positive ionization," *J. Chem. Phys.*, vol. 43, no. 5, pp. 1464–1479, 1965.

[18] D. Mathur and C. Badrinathan, "Ionization of xenon by electrons: Partial cross sections for single, double, and triple ionization," *Phys. Rev. A*, vol. 35, no. 3, pp. 1033–1042, Feb. 1987.

[19] C. A. Lentz, "Transient one dimensional numerical simulation of Hall thrusters," M.S. thesis, Dept. Aeronautics Astronautics, Massachusetts Inst. Technol., Cambridge, MA, USA, 1990.

[20] C. A. J. Fletcher, *Computational Techniques for Fluid Dynamics 1*, 2nd ed. New York, NY, USA: Springer-Verlag, 1991.

[21] N. B. Meezan, "Electron transport in a coaxial Hall discharge," Ph.D. dissertation, Dept. Mech. Eng., Stanford Univ., Stanford, CA, USA, 2002.

[22] N. B. Meezan and M. A. Cappelli, "Kinetic study of wall collisions in a coaxial Hall discharge," *Phys. Rev. E*, vol. 66, no. 3, p. 036401, 2002.

[23] C. Hirsch, *Numerical Computation of Internal and External Flows: The Fundamentals of Computational Fluid Dynamics*, 2nd ed. Oxford, U.K.: Butterworth-Heinemann, 2007, pp. 141–209.

[24] A. Simon, "Instability of a partially ionized plasma in crossed electric and magnetic fields," *Phys. Fluids*, vol. 6, no. 3, pp. 382–388, 1963.

[25] Y. B. Esipchuk, A. I. Morozov, G. N. Tilinin, and A. V. Trofimov, "Plasma oscillations in closed-drift accelerators with an extended acceleration zone," *Soviet Phys. Tech. Phys.*, vol. 18, no. 7, pp. 928–932, 1974.

[26] V. I. Baranov, Y. S. Nazarenko, V. A. Petrosov, A. I. Vasin, and Y. M. Yashonov, "Theory of oscillations and conductivity for Hall thruster," presented at 32nd AIAA/ASME/SAE/ASEE Joint Propuls. Conf. AIAA, Lake Buena Vista, FL, USA, Jul. 1996, paper 96-3192.

Cheryl M. Lam received the B.S. and M.S. degrees in electrical engineering from Stanford University, Stanford, CA, USA, in 2002 and 2003, respectively, where she is currently pursuing the Ph.D. degree in mechanical engineering.

She returned to the Stanford Plasma Physics Laboratory at Stanford University as a Ph.D. student, in 2007, with a focus on the numerical simulation of plasma discharges, in particular, Hall thrusters and similar plasma devices. She is currently a Senior Research and Development Scientist with Sandia National Laboratories, Livermore, CA, USA. Her current research interests include large-scale integrated electrical and multi-physics simulations and computational model verification and validation.

Eduardo Fernandez received the B.S. degree in physics and mathematics from the University of Wisconsin–Eau Claire, Eau Claire, WI, USA, and the Ph.D. degree in physics from the University of Wisconsin–Madison, Madison, WI, USA.

He is currently a Professor of Physics and Mathematics with Eckerd College, St. Petersburg, FL, USA. His current research interests include plasma physics, in particular, simulation of magnetized low-temperature plasmas used in electric propulsion applications, and turbulence in fusion plasmas.

Mark A. Cappelli received the B.A.Sc. degree in physics from McGill University, Montreal, QC, Canada, in 1980, and the M.A.Sc. and Ph.D. degrees in aerospace science and engineering from the University of Toronto, Toronto, ON, Canada, in 1983 and 1987, respectively.

He is currently a Professor with the Department of Mechanical Engineering, Stanford University, Stanford, CA, USA. His current research interests include plasmas and gas discharges as they apply to aerodynamic and space propulsion, combustion, electromagnetics, and material processing.